



# Modelling of FDG metabolism in liver voxels



C. Baker<sup>a,b,\*</sup>, N. Dowson<sup>a</sup>, P. Thomas<sup>b,c</sup>, S. Rose<sup>a</sup>

<sup>a</sup> The Australian e-Health Research Centre, Royal Brisbane and Women's Hospital, Herston, 4029 Queensland, Australia

<sup>b</sup> School of Medicine, The University of Queensland, 288 Herston Road, Herston, 4006 Queensland, Australia

<sup>c</sup> Specialised PET Services, Nuclear Medicine Department, Royal Brisbane and Women's Hospital, Herston, 4029 Queensland, Australia

## HIGHLIGHTS

- When parameterising biology the fidelity of the output parameters is important.
- Current models obtain low residuals but seldom reflect underlying biology precisely.
- We introduce a model informed by physiological features particular to the liver.
- The model better agrees with established blood volume and perfusion data.
- Improvements in image contrast has practical implications for clinical reporting.

## ARTICLE INFO

### Article history:

Received 11 May 2014

Received in revised form

21 October 2014

Accepted 23 October 2014

Available online 11 November 2014

### Keywords:

Mathematical liver physiology

Kinetic analysis

Compartment modelling

Parametric imaging

Positron emission tomography

## ABSTRACT

Kinetic analysis is a tool used to glean additional information from positron emission tomography (PET) data by exploiting the dynamics of tissue metabolism. The standard irreversible and reversible two compartment models used in kinetic analysis were initially developed to analyse brain PET data. The application of kinetic analysis to PET of the liver presents the opportunity to move beyond the generic standard models and develop physiologically informed pharmacokinetic models that incorporate structural and functional features in particular to the liver. In this paper, we develop a new compartment model, called the tubes model, which is informed by the liver's sinusoidal architecture, high fractional blood volume, high perfusion rate, and large hepatocyte surface area facing the space of Disse. The tubes model distributes tracer between the blood and intracellular compartments in more physiologically faithful proportions than the standard model, producing parametric images with improved contrast between healthy and neoplastic tissue.

Crown Copyright © 2014 Published by Elsevier Ltd. All rights reserved.

## 1. Introduction

Kinetic analysis involves fitting a pharmacological model of tracer metabolism to PET data, the outcome of which is a collection of kinetic parameters describing the dynamics of tissue metabolism in each voxel. The kinetic parameters can be visualised in various ways to produce parametric images of the PET data. Although kinetic analysis has proven to be a powerful tool in the development of new PET tracers, long computation times and difficulties in reliably interpreting kinetic parameters hamper the quotidian use of parametric images in clinical practice. The detection of small liver lesions is, however, particularly suited to kinetic analysis because of marked biological differences in the way healthy and neoplastic liver tissue processes

fluorodeoxyglucose (FDG). In contrast to healthy liver tissue, which rapidly takes up and extrudes FDG, neoplastic liver tissue retains the metabolised FDG. Despite differences in biology, some of the distinction between liver tissue and small lesions is lost when viewing static PET images. Small lesions can be difficult to distinguish because normal liver tissue also has high uptake and PET images typically have a large point spread function (full width half max of 5–10 mm). Kinetic analysis is able to glean further information from static PET data by exploiting the dynamics of tissue metabolism.

The standard irreversible and reversible two compartment models were developed in Sokoloff et al. (1977) and Phelps et al. (1979), respectively, to analyse brain PET data. The application of kinetic analysis to PET of the liver offers the opportunity to revise the standard compartment models to take into consideration particular structural and functional features of the liver. For example, the liver is one of the most highly perfused and vascular organs of the body, receiving 20–25% of cardiac output and being 25–30% blood by volume (Arias et al., 2011; Lautt, 2009). By

\* Corresponding author at: The Australian e-Health Research Centre, Royal Brisbane and Women's Hospital, Herston, 4029 Queensland, Australia.

E-mail address: [Charles.Baker@csiro.au](mailto:Charles.Baker@csiro.au) (C. Baker).

comparison, the brain is about 5% blood by volume (Leenders et al., 1990). Consequently, much more activity in a liver voxel is contained in the blood compartment.

An important step in the development of physiologically informed liver kinetic modelling is the introduction of a dual hepatic artery-portal vein input function by Munk et al. (2001). A further step beyond the standard model is taken by Munk et al. (2003), where they model the blood compartment as a single tube, producing a first-order transport equation for the blood concentration, and obtain an analytic solution assuming that no back-flux from the tissue compartment into the blood compartment occurs. In the presence of back-flux they propose an elegant approximation: an interpolation between no back-flux at short time scales and the steady-state solution at long time scales.

In this paper, we develop a physiologically informed compartment model, called the tubes model, that incorporates structural and functional features in particular to the liver. A key feature of the tubes model is the modelling of sinusoidal architecture by a series of tubes. The use of tubes to model sinusoids at the voxel level is motivated by the rich literature concerning the mathematical modelling of gross hepatic elimination of drugs, where the entire liver, as opposed to a single voxel, is modelled as a collection of tubes. A survey of the mathematical modelling of gross liver kinetics can be found in Anissimov (1998). The work of Goresky (1963) is an important milestone in the mathematical modelling of gross liver kinetics. In that article, Goresky introduces a number of ideas that remain central to more complex models that have been developed thereafter, in particular, the use of tubes to model sinusoids, and the assumption that convective mass transfer dominates diffusive mass transfer in liver sinusoids. Following Goresky's work, a number of more complex models have been developed to better approximate the underlying liver physiology, including the parallel tubes model of Bass et al. (1976), which models the liver as a number of identical parallel tubes, and the distributed model of Bass et al. (1978), which accounts for functional heterogeneity in steady-state situations by modelling a distribution of reaction rates. Most recently, the interconnected tubes model of Anissimov et al. (1997) takes another step by modelling the interconnection of sinusoids. The physiologically informed development of the models of gross liver pharmacokinetics has inspired us to attempt to “bring physiology to PET of the liver” (Keiding, 2012).

The layout of this paper is as follows: In the following section, we describe the standard model, its analytic solution, and the fitting process for determining reaction rate constants from measured PET data. In the third section we introduce the tubes model. The tubes model incorporates three particular features of liver structure and function. First, sinusoidal architecture is captured by modelling a voxel as a collection of parallel one-dimensional tubes. Second, the tubes model takes into consideration the liver's high perfusion rate by modelling blood flow through the parallel tubes as porous media flow with the aid of Darcy's Law. Lastly, the liver's high fractional blood volume is accounted for by apportioning a fraction of the total voxel blood volume to larger vessels of the hepatic vascular tree which are not in direct contact with the sinusoidal plates. After the tubes model is introduced, in Section 4 we discuss the model solutions and compare parametric images computed from an axial slice of PET data. A list of mathematical symbols is contained in Appendix A.

## 2. Kinetic analysis and the standard model

We begin by briefly introducing the standard model and the parameter fitting process. An introduction to kinetic analysis of PET data can be found in Carson (2005). In the standard

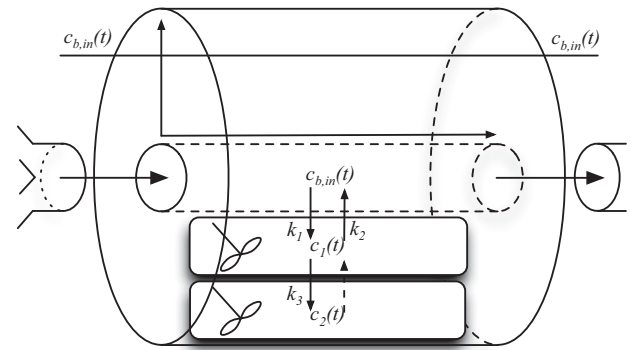


Fig. 1. Standard model of a liver voxel.

two-compartment model, blood containing FDG flows into a voxel at a concentration  $c_{b,in}$ , where it is transported at a rate  $k_1$  into the first intracellular compartment, attaining a concentration of  $c_1(t)$  at time  $t$ . From the first intracellular compartment, FDG can enter the second intracellular compartment, where it assumes a concentration  $c_2(t)$ , by being phosphorylated at a rate  $k_3$  to FDG-6-P by hexokinase, or it can be transported back into the blood compartment at a rate  $k_2$ . In the reversible model, FDG-6-P can re-enter the first intracellular compartment after being dephosphorylated at a rate  $k_4$  by glucose-6-phosphatase. The standard model is represented pictorially in Fig. 1.

The standard model equations with reversible kinetics are

$$\begin{aligned} \frac{d}{dt}c_1(t) &= k_1c_{b,in} - (k_2 + k_3)c_1 + k_4c_2 \\ \frac{d}{dt}c_2(t) &= k_3c_1 - k_4c_2. \end{aligned} \quad (1)$$

We denote the voxel volume by  $V_{vox}$  and the fraction of blood compartment volume over voxel volume by  $f_b$ , which has units of mL of blood per mL of voxel. We sometimes refer to  $f_b$  as the fractional blood volume or FBV. The volume of the blood compartment is then  $f_bV_{vox}$  mL and the volume of both intracellular compartments is  $(1 - f_b)V_{vox}$  mL. The total voxel activity measured by a PET scanner is the sum of activity in both the intracellular compartments and the blood compartment.

The process of fitting a model to measured PET data is usually achieved by weighted nonlinear least squares optimisation using either the Levenberg–Marquardt or Powell dogleg methods (Levenberg, 1944; Marquardt, 1963; Powell, 1970). For each voxel, we are given a time activity curve (TAC) in the form  $y(t_i) = y^i$ ,  $i = 1, \dots, N$ , where  $t_i$  are the time points at which the images are acquired and  $N$  is the total number of time points. Examples of TACs are shown in Fig. 7. Noise in PET data is commonly modelled by a Poisson distribution in which case the weights are  $w_i = 1/\sqrt{y^i}$  (Carson, 2005). The optimisation problem for the standard model is to minimise the weighted sum of squares:

$$\min_{k_1, k_2, k_3, k_4} \frac{1}{2} \sum_{i=1}^N \left( w_i y^i - (1 - f_b)(c_1^i(k_1, k_2, k_3, k_4) + c_2^i(k_1, k_2, k_3, k_4)) - f_b c_{b,in}^i \right)^2$$

over the rate constants  $k_1, k_2, k_3, k_4$  and fractional blood volume  $f_b$ . The concentrations  $c_1(t)$  and  $c_2(t)$  are found by solving the model system (1) either analytically or numerically. As the above equation indicates, the standard model solutions for  $c_1(t)$  and  $c_2(t)$  depend only on  $k_1, k_2, k_3, k_4$  and not on  $f_b$ .

As we have mentioned, the standard model with irreversible kinetics was introduced by Sokoloff et al. (1977) to study tracer metabolism in the brain. Later, the standard model was extended

to irreversible kinetics by Phelps et al. (1979) to account for the small amount of glucose-6-phosphatase present in healthy brain tissue. The activity of glucose-6-phosphatase in healthy liver is greater than that of healthy brain (Munk et al., 2001; Phelps et al., 1979), and as such, models with reversible kinetics could better model FDG metabolism in healthy liver tissue in the latter stages of longer scans.

Notwithstanding the physiological presence of glucose-6-phosphatase in the liver, we believe that there are advantages in using a simpler irreversible model. Model fit residual is usually decreased by adding additional model parameters, and a balance must be struck between the number of model parameters and residual error so as not to over-fit the data or erroneously conclude that meaningful information is contained in the additional parameters. A well-known statistical criterion for determining the optimum number of model parameters is the Akaike Information Criterion (AIC) (Akaike, 1998), which includes a penalty function for increasing numbers of model parameters. We compared the standard model with reversible and irreversible kinetics with the AIC and found that although the introduction of the  $k_4$  parameter marginally reduces the fit residual, the irreversible model is more favourable in terms of AIC. Comparison of the standard and tubes models with the AIC is presented in Table 3 of Section 4. The reduction in model fit residual produced by reversible kinetics only occurs in the last 20 min of hour long scans; during the first 40 min in healthy liver tissue, and in other tissues at all times, tracer metabolism is well-modelled by irreversible kinetics. Even in the final 20 min of hour long scans irreversible kinetic still provides an accurate approximation of tracer dynamics. Fig. 6 in Section 4 presents standard and tubes model fits (with irreversible kinetics) for a typical healthy liver TAC. From a mathematical perspective, the assumption of irreversible kinetics allows one to explicitly solve the tubes model equations. On the basis of these observations, we concluded that irreversible kinetics provides a reasonable approximation to liver kinetics, and from now on we assume  $k_4 = 0$  and work only with irreversible kinetics.

The assumption that  $k_4 = 0$  uncouples the system (1) and the equations can be solved separately. The first equation is linear in  $c_1(t)$  and is easily solved in the usual way using an integrating factor. The second equation can then be solved by substituting in the solution for  $c_1(t)$  and integrating. The solution to the system with initial conditions  $c_1(0) = c_2(0) = 0$  is

$$\begin{aligned} c_1(t) &= k_1 \int_0^t e^{-(k_2+k_3)\tau} \cdot c_{b,in}(t-\tau) d\tau \\ c_2(t) &= \frac{k_1 k_3}{k_2 + k_3} \int_0^t \left(1 - e^{-(k_2+k_3)\tau}\right) \cdot c_{b,in}(t-\tau) d\tau. \end{aligned} \quad (2)$$

We point out that two basic assumptions of the standard model are that (1) there is no back-flux of tracer from the first intracellular compartment to the blood compartment; and (2) the amount of tracer in blood is much larger than the amount of tracer entering the first intracellular compartment, and therefore tracer concentration everywhere in the blood compartment is approximately equal to the blood input function  $c_{b,in}(t)$ . As pointed out in Munk et al. (2012), these assumptions are not physiologically accurate. The tubes model avoids making these unphysiological assumptions by returning tracer back-flux into the blood compartment and allowing blood concentration to vary down the length of the sinusoidal tubes.

As a final comment before introducing the tubes model, we mention that kinetic analysis of PET data has much in common with kinetic analysis of dynamic contrast-enhanced magnetic resonance data (DCE MRI). The use of kinetic analysis in DCE MRI is more developed than in PET, and models more complex than the standard model (the equivalent of the standard model in DCE MRI is called the Tofts et al., 1999 model) are used to fit kinetic

parameters to DCE MRI images although the technique is still not commonly used in clinical practice. A review of kinetic analysis in DCE MRI can be found in Sourbron and Buckley (2012). Notwithstanding the similarities, the application of kinetic analysis to PET data presents a number of challenges not encountered in DCE MRI. The kinetic models used in DCE MRI are usually one-compartment models, representing an intravascular compartment and an extravascular compartment, and the permeability-surface product is usually assumed to be same in either direction. The kinetic models used in FDG PET require a second intracellular compartment to model the phosphorylation of FDG to FDG-6-P, introducing the reaction rate  $k_3$  as in Fig. 1. A further issue is that PET data is inherently noisier than DCE MRI data, complicating the fitting process.

### 3. The tubes model

Our interest in developing the new tubes model is to improve the standard model by taking into consideration a number of structural and functional features of the liver. In particular, we wish to model the liver's (1) sinusoidal architecture, (2) high fractional blood volume and (3) high perfusion rate. A further issue that arises is the surface area available for GLUT2 transporters to occupy.

We first recall some relevant features of the liver's structural organisation and haemodynamics, and direct the interested reader to Arias et al. (2011) and Lautt (2009) for more details. The liver parenchyma is classically represented as a mosaic of hexagonal shaped lobules, each centred about a hepatic venule with terminal branches of the hepatic artery and portal vein located at the six vertices. The sinusoids are vascular channels that run from the vertices of the hexagonal lobules to the centrally located venules. Arterial and portal blood mixes at the proximal end of the sinusoids, traverses the sinusoids and empties into the hepatic venules, eventually returning to the right side of the heart via the hepatic veins and inferior vena cava. The dimensions of a hepatic lobule are roughly the size of a voxel, with measurements varying around  $2 \text{ mm} \times 0.7 \text{ mm}$ , the length of a sinusoid being half the short dimension or  $0.25\text{--}0.5 \text{ mm}$ .

The liver receives a dual blood supply, roughly one-third to one-fifth from the hepatic artery, with the remaining fraction being supplied by the portal vein (Lautt, 2009). The two vessels arrive at the porta hepatis and then ramify throughout the liver, with arterial and venous blood finally being mixed when terminal hepatic arterioles and portal venules empty into the periportal end of sinusoids. The passage of blood from inside a sinusoid to the interior of a hepatocyte involves few steps: blood plasma containing FDG leaves the sinusoidal lumen through fenestrations in the vessel wall and enters the space of Disse. The sinusoidal fenestrations are small enough not to permit the passage of red blood cells. From the space of Disse, FDG is transported into hepatocytes, and from the hepatocyte back to the space of Disse, by bidirectional transmembrane GLUT2 transporters.

Motivated by the tubular models of gross hepatic drug elimination (Goresky, 1963; Bass et al., 1976, 1978; Anissimov et al., 1997), we capture the tubular sinusoidal architecture by modelling a liver voxel as a collection of parallel tubes. We do not assume that the tubes are well-mixed compartments in order to allow variation of concentration down the length of sinusoids. Hepatocytes are known to display functional heterogeneities depending on their location along the length of sinusoids. In particular, glucose metabolism varies between the oxygen rich periportal zone and the oxygen depleted centrilobular zone (Arias et al., 2011). The existence of sinusoidal concentration gradients has been confirmed by Weisiger et al. (1986) in experiments

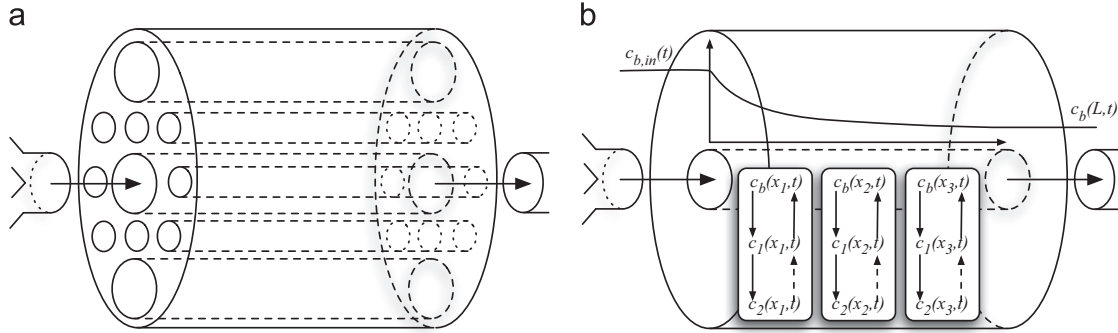


Fig. 2. The tubes model. (a) Conceptualisation of a liver voxel. (b) The Tubes model (only one tube shown).

measuring the uptake of thyroxine in rat liver. The tubes model is represented pictorially in Fig. 2.

We now derive the governing equations of the tubes model. Consider a collection of parallel sinusoidal tubes, denoted by  $B$ , of length  $L$  and volume  $V_s$ . Suppose tracer flows into the sinusoidal tubes at a constant flow rate  $F_s$  and concentration  $c_{b,in}(t)$ , attaining a concentration at point  $x \in [0, L]$  of  $c_s(x, t)$ . Denote by  $j(x, t)$  the flux of tracer through the boundary  $\partial B$  of the tubes, and by  $r(x, t)$  a reaction term, either negative for removal of tracer from the blood compartment or positive for back-flux into the blood compartment. A mass balance over  $B$  and its boundary  $\partial B$  is of the form

$$\frac{d}{dt} \int_B c_s(x, t) dV_s = - \int_{\partial B} j(x, t) \cdot n dS_s + \int_B r(x, t) dV_s, \quad (3)$$

where  $n$  denotes the unit normal to the surface, directed outwards, so with the negative sign the first term on the right corresponds to inwards flux. In general, the total flux across the boundary has both diffusive and convective components. Fick's law of diffusion states that the diffusive flux is equal to

$$j_{\text{diff}} = -D \partial_x c_s(x, t),$$

where  $D$  is the coefficient of diffusion of the tracer. The convective flux through  $\partial B$  is given by the mass flow rate  $F_s \cdot c_s(x, t)$  divided by the cross-sectional area  $A_s$  of the sinusoidal tubes, or  $j_{\text{conv}} = v c_s(x, t)$ , where  $v = F_s / A_s$  is the sinusoidal perfusion velocity in cm/min. Combining the diffusive and convective fluxes, the total mass flux is

$$j = -D \partial_x c_s(x, t) + v c_s(x, t).$$

Assuming average experimental values for the geometry of sinusoids and perfusion rate, calculation of the Peclet number reveals a characteristic convection time of a few seconds and a characteristic diffusion time of greater than 100 s (Goresky, 1963; Anissimov et al., 1997). As a consequence, diffusion does not contribute significantly to the transport of FDG down a sinusoid, and hereafter we assume  $D=0$ . A well-known model of gross liver kinetics, the dispersive model of Roberts and Rowland (1986), includes a second order derivative term, not to model molecular diffusion but rather additional bulk mixing or dispersion effects created by the interconnection of sinusoids. Such a dispersion term could be included in the tubes model at the cost of having to specify an additional constant, and considerably complicating the mathematics.

After entering the sinusoids, tracer is transported out of the sinusoidal blood compartment into the tissue compartment at a rate  $\tilde{k}_1$  proportionate to the sinusoidal blood tracer concentration  $c_s(x, t)$  and the surface area available for reaction  $A_{rxn}$ . Once inside the first intracellular compartment, tracer is transported back into the sinusoidal blood compartment at a rate  $\tilde{k}_2$  proportionate to the concentration in the intracellular compartment  $c_1(t)$ , and the surface area available for reaction is the same. Thus, the total reaction term for the blood compartment is  $-\tilde{k}_1 A_{rxn} / V_s c_s(x, t) + \tilde{k}_2 A_{rxn} / V_s c_1(x, t)$ . Substituting

the convective flux and reaction terms into the mass balance (3) gives

$$\begin{aligned} \frac{d}{dt} \int_B c_s(x, t) dV_s = & - \int_{\partial B} v c_s(x, t) dS_s \\ & + \int_B \left( -\frac{\tilde{k}_1 A_{rxn} c_s(x, t)}{V_s} + \frac{\tilde{k}_2 A_{rxn} c_1(x, t)}{V_s} \right) dV_s, \end{aligned}$$

and with the aid of the Gauss divergence theorem (see, for example, Hildebrand, 1976),

$$\int_{\partial B} v c_s(x, t) dS_s = \int_B v \partial_x c_s(x, t) dV_s,$$

we obtain the tubes model equation for the sinusoidal blood compartment:

$$\partial_t c_s(x, t) = -v \partial_x c_s(x, t) - \frac{\tilde{k}_1 A_{rxn}}{V_s} c_s(x, t) + \frac{\tilde{k}_2 A_{rxn}}{V_s} c_1(x, t). \quad (4)$$

The blood flow rate  $F$  has units of mL/min and the perfusion rate  $q$  has units of mL/min/g of liver. The perfusion rate of the liver is, on average, about 1.0–1.3 mL/min/g of liver (Arias et al., 2011; Lautt, 2009). As a comparison, the perfusion rate of the brain is, on average, about 0.5 mL/min/g of brain (Leenders et al., 1990). The blood flow rate  $F$  is expressed in terms of the perfusion rate  $q$  by  $F = q \cdot \rho_{\text{liver}} \cdot V_{\text{vox}}$ . For convenience we shall assume  $\rho_{\text{liver}} = 1$  g/mL and hence  $F = q \cdot V_{\text{vox}}$ . The concentrations have units of kBq/mL.

We now want to incorporate the liver's high fractional blood volume and perfusion rate into the above equations. The sinusoids make up about 60% of the total liver blood volume, equating to about 15% of total liver volume, with larger vessels of the hepatic vascular tree making up the remaining 40% (Arias et al., 2011). The total volume of blood in a voxel  $V_b = f_b V_{\text{vox}}$  mL is thus the sum of the sinusoidal blood volume  $V_s$  and the large vessel blood volume  $V_l$ , where  $V_s = 0.6 f_b V_{\text{vox}}$  mL and  $V_l = 0.4 f_b V_{\text{vox}}$  mL. We assume that blood in the larger vessels has not participated in FDG metabolism at the sinusoidal plates, and therefore has a concentration profile similar to the blood input function  $c_{b,in}$ . Denote by  $\bar{c}_s(t)$  the average value of sinusoidal blood concentration:

$$\bar{c}_s(t) = \frac{1}{L} \int_0^L c_s(x, t) dx,$$

and by  $c_b$  the total concentration of blood in a voxel. The total concentration of blood in voxel, being a combination of the metabolically active sinusoidal blood and the blood input function, is then given by

$$c_b(t) = 0.4 c_{b,in}(t) + 0.6 \bar{c}_s(t). \quad (5)$$

The tubular sinusoidal architecture leads us to consider a voxel as a porous medium of tissue and vasculature, where  $f_b$  corresponds to the porosity, and to model blood flow rate through the voxel with the aid of Darcy's Law. In our setting, Darcy's Law states



that the blood flow rate  $F$  to a voxel is determined by

$$F = \frac{f_b L^2}{\mu} \frac{dP}{dL}, \quad (6)$$

where  $\mu$  the blood viscosity and  $dP/dL$  the pressure gradient across a voxel. We assume that the pressure gradient is constant (the pressure drop across sinusoids is about 5 mmHg [Lautt, 2009](#)), substitute  $F = qV_{\text{vox}}$  mL/min, and lumping various constants into a single constant  $\alpha$  we find that the perfusion rate to a voxel is  $q = \alpha f_b$  mL/min/g of liver. The constant  $\alpha$  can be determined by experimental data or, potentially, could also be fitted to measured data. As we have previously stated, on average, the liver is perfused at rate of between 1–1.3 mL/min/g of liver and is 25–30% blood by volume. We assume, for convenience, figures of 1.3 mL/min/g of liver and 26%. Consequently, when  $f_b = 0.26$  we expect  $q = 1.3$ , which gives  $q = 5f_b$  mL/min/g of liver. We see the use of Darcy's Law to model blood flow through a voxel results in a linear dependence of the perfusion rate on the fraction blood volume. We are not aware of any experimental data in the liver supporting this relationship, although experimental data in the brain does confirm a linear relationship between perfusion rate and FBV ([Rostrup et al., 2005](#)). Note that  $\alpha$  is just the inverse of the mean residence time of tracer in a voxel  $\bar{\tau} = V_b/F$ . As the sinusoids receive only 60% of the total blood flow to a voxel, the sinusoidal perfusion flow rate is  $q_s = 0.6\alpha f_b$  mL/min/g of liver. The cross-sectional area of the sinusoids,  $A_s$ , is related to the sinusoidal blood volume by  $A_s L = 0.6f_b V_{\text{vox}}$ , and hence the sinusoidal perfusion velocity is

$$v = \frac{F_s}{A_s} = \alpha L.$$

The last point to address in the derivation of the tubes model equation for the sinusoidal blood compartment is the dependency of the surface area available for reaction on the volume of the sinusoidal blood compartment. Here, we are again guided by liver physiology. As we are modelling the sinusoids as tubes, the sinusoidal wall area is  $2\pi RLN$ , where  $R$  is the radius of the tubes,  $L$  the tube length and  $N$  the number of tubes. The sinusoidal blood volume is  $\pi R^2 LN = 0.6f_b V_{\text{vox}}$ , and thus the endothelial wall area is  $2/R \cdot 0.6f_b V_{\text{vox}}$ . This is not, however, the surface area available for GLUT2 transporters to occupy because blood plasma first extravasates into the space of Disse, bathing the hepatocytes in blood. About 35% of the total hepatocyte surface faces sinusoids, and the area of this surface is greatly increased by microvilli that extend into the space of Disse ([Arias et al., 2011](#)), providing a surface area of reaction far greater than the tubular endothelial wall area. In principle, it is possible to model to rate of transport into the space of Disse separately, but at the expense of an additional kinetic parameter, the true permeability-surface product of sinusoids. As we want to avoid introducing an additional parameter, we assume that tracer enters the space of Disse much faster than the rate at which GLUT2 transporters take up FDG, and thus tracer concentration inside the space of Disse is approximately equal to tracer concentration inside sinusoids. By making this assumption, we are treating the intravascular space and the extravascular space of Disse as a single blood compartment. We shall return to this point in [Section 4](#). Secondly, as the surface area of the hepatocytes exposed to blood plasma in the space of Disse is extremely large, we assume that the area available for reaction  $A_{rxn}$  is independent of  $f_b$ .

As the constants  $\tilde{k}_i A_{rxn}/V_{\text{vox}}$  for  $i = 1, 2$  always appear together, to simplify notation we set  $k_i = \tilde{k}_i A_{rxn}/V_{\text{vox}}$ . We incorporate the equations  $V_s = 0.6f_b V_{\text{vox}}$  and  $v = \alpha L$  into (4) to obtain the tubes model equation for the sinusoidal blood compartment:

$$\frac{\partial}{\partial t} c_s(x, t) = -\alpha L \frac{\partial}{\partial x} c_s(x, t) - \frac{k_1}{0.6f_b} c_s(x, t) + \frac{k_2}{0.6f_b} c_1(x, t). \quad (7)$$

We now move on to derive the tubes model equations for the two intracellular compartments. As we have said, once inside the

first intracellular compartment, tracer is transported back into the blood compartment at a rate  $\tilde{k}_2$  proportionate to the concentration in the intracellular compartment  $c_1(x, t)$ , and the surface area available for reaction  $A_{rxn}$ . Within the tissue compartment, FDG is phosphorylated at a rate  $k_3$  to FDG-6-P, assuming a concentration  $c_2(x, t)$ . A mass balance over the intracellular compartments gives

$$\begin{aligned} V_1 \frac{d}{dt} c_1(x, t) &= \tilde{k}_1 c_s(x, t) A_{rxn} - \tilde{k}_2 c_1(x, t) A_{rxn} - k_3 c_1(x, t) V_1 \\ V_2 \frac{d}{dt} c_2(x, t) &= k_3 c_1(x, t) V_2. \end{aligned} \quad (8)$$

Although the model refers to two intracellular compartments, we assume that FDG and FDG-6-P are free to occupy the entirety of the intracellular space, and hence  $V_1 = V_2 = (1 - f_b) V_{\text{vox}}$ . After substituting  $V_1 = V_2 = (1 - f_b) V_{\text{vox}}$  and  $k_i = \tilde{k}_i A_{rxn}/V_{\text{vox}}$  into (8), the complete set of tubes model equations is

$$\begin{aligned} \frac{\partial}{\partial t} c_s(x, t) &= -\alpha L \frac{\partial}{\partial x} c_s(x, t) - \frac{k_1}{0.6f_b} c_s(x, t) + \frac{k_2}{0.6f_b} c_1(x, t) \\ \frac{d}{dt} c_1(x, t) &= \frac{k_1}{(1 - f_b)} c_s(x, t) - \frac{k_2}{(1 - f_b)} c_1(x, t) - k_3 c_1(x, t) \\ \frac{d}{dt} c_2(x, t) &= k_3 c_1(x, t), \end{aligned} \quad (9)$$

and the total voxel blood concentration measured by the PET scanner is

$$c_b(t) = 0.4c_{b,in}(t) + 0.6 \cdot \frac{1}{L} \int_0^L c_s(x, t) dx.$$

A simplification to the system (9) can be made by assuming that  $k_2 = 0$  and the intracellular compartment sees an average of the sinusoidal blood concentration. The first assumption uncouples the equations for  $c_s(t)$  and  $c_1(x, t)$  of (9), allowing the equation for  $c_s$  to be solved separately; and the second assumption removes the dependency of  $c_1$  and  $c_2$  on the spatial variable  $x$ . The assumption that  $k_2 = 0$  is approximately valid, for instance, at short times after the introduction of tracer. Having made these assumptions, the equation for the sinusoidal blood concentration becomes

$$\frac{\partial}{\partial t} c_s(x, t) = -v \frac{\partial}{\partial x} c_s(x, t) - \frac{k_1}{0.6f_b} c_s(x, t). \quad (10)$$

Making the substitution  $u(x, t) = c_s(x, t) e^{k_1/(v \cdot 0.6f_b)x}$  converts (10) into the first-order wave equation  $\partial_t u(x, t) = -v \partial_x u(x, t)$ , the solution of which is

$$c_s(x, t) = c_{b,in}(t - x/v) e^{-k_1/(v \cdot 0.6f_b)x},$$

giving an average sinusoidal concentration  $\bar{c}_s$  of

$$\bar{c}_s(t) = \frac{1}{L} \int_0^L c_{b,in}(t - x/v) e^{-k_1/(v \cdot 0.6f_b)x} dx.$$

A similar equation is obtained by [Munk et al. \(2003\)](#) for the blood compartment, as distinct from the sinusoidal blood compartment.

The special sinusoidal architecture naturally suggests the use of tubes to model a liver voxel, however, blood flow through other organs can reasonably be modelled as flow and reaction down the length of tubes. The passage of blood flow through the spleen, for example, is through the splenic sinusoids and cords of the red pulp. The parametric images presented in [Fig. 11a–f](#) are computed from an axial slice of PET data through the liver and spleen. We are not aware of any experimental measurements of the fraction of splenic blood volume residing in large vessels, so in the absence of this information, we model a splenic voxel by the tubes equations but without making the adjustment for a fraction of blood residing in metabolically inactive large vessels. The simplified set of tubes

equations we use to model a splenic voxel is

$$\begin{aligned}\frac{\partial}{\partial t}c_b(x, t) &= -\alpha L \frac{\partial}{\partial x}c_b(x, t) - \frac{k_1}{f_b}c_b(x, t) + \frac{k_2}{f_b}c_1(x, t) \\ \frac{d}{dt}c_1(x, t) &= \frac{k_1}{(1-f_b)}c_b(x, t) - \frac{k_2}{(1-f_b)}c_1(x, t) - k_3c_1(x, t) \\ \frac{d}{dt}c_2(x, t) &= k_3c_1(x, t).\end{aligned}\quad (11)$$

We now return to solve the full system (9). The assumption of irreversible kinetics uncouples the equation for  $c_2$ , leaving a coupled system of two equations for  $c_b$  and  $c_1$ . The explicit solution of a coupled system of two linear parabolic equations has been obtained by Hill (1981) via clever transform methods. To simplify notation, set

$$\begin{aligned}a &:= k_1/(0.6f_b) & c &:= k_1/(1-f_b) \\ b &:= k_2/(0.6f_b) & d &:= k_2/(1-f_b) + k_3\end{aligned}$$

and

$$\eta := 2\sqrt{bc\tau(t-\tau)}.$$

After making the notational changes, the solution of the tubes model equations for  $c_s(x, t)$  and  $c_1(x, t)$  provided by Hill's formulae is

$$\begin{aligned}c_s(x, t) &= e^{-at}c_{b,in}(t-x/v) \\ &+ \sqrt{bc} \cdot e^{-dt} \int_0^t e^{-(a-d)\tau} \sqrt{\frac{\tau}{t-\tau}} \cdot I_1(\eta)c_{b,in}(\tau-x/v) d\tau \\ c_1(x, t) &= ce^{-dt} \int_0^t e^{-(a-d)\tau} I_0(\eta)c_{b,in}(\tau-x/v) d\tau,\end{aligned}\quad (12)$$

where  $I_0$  and  $I_1$  are the modified Bessel functions (Abramowitz and Stegun, 1964). The blood input function can be well-approximated by a sum of exponential functions  $c_{b,in}(t) = \sum_i A_i e^{-\kappa_i t}$  (Feng et al., 1993; Munk et al., 2003) in which case the above integrals can be explicitly computed. These computations are carried out in Appendix B. We now have three ways of solving the tubes model: (1) fit a sum of exponentials to the blood input function and solve analytically using the equations in Appendix B, (2) use Eqs. (12) and numerically integrate using the trapezoid rule or (3) solve the system (9) numerically, for example using the method of lines (Griffiths, 2009).

#### 4. Discussion of numerical results

In this section we discuss the model solutions with the aid of parametric images computed from an axial slice of dynamic PET data through the liver and spleen of a human patient. PET imaging was performed using a Philips Gemini GXL PET/CT scanner. The patient fasted for 6 h prior to scanning. Following a transmission CT scan, while remaining in the scanner, the patient was intravenously administered a single FDG bolus with an activity of 319 MBq. PET scanning was initiated immediately prior to injection in order to estimate the blood input function. A total of 19 image volumes were acquired during the 60 min scan at the time points  $t \in \{1/6, 2/6, 3/6, 4/6, 5/6, 1, 1.5, 2, 2.5, 3, 4, 5, 10, 15, 20, 30, 40, 50, 60\}$ . The images were reconstructed using ordered subset expectation maximisation with corrections for attenuation and scatter. No additional post-filtering was performed. The measured resolution of the scanner has been reported to range from  $5.4 \times 5.4 \times 6.0$  mm at the centre of the field of view to  $6.1 \times 6.1 \times 6.6$  mm when offset 10 cm in the axial and transverse directions (Sathiakumar et al., 2010). The images were reconstructed with a voxel spacing of  $4 \times 4 \times 3$  mm<sup>3</sup>. Kinetic analysis of the chosen slice of PET data was computed in Matlab on a

MacBook with a 2.4 GHz Intel Core 2 Duo processor and 4 GB 667 MHz DDR2 SDRAM.

The static PET image was used to cluster voxels into four regions of interest (ROIs): healthy liver, neoplastic liver, necrotic liver and spleen; and then all TACs within each region were averaged to obtain four representative TACs, one from each region. The static PET image of the chosen slice is presented in Fig. 3, the tissue ROIs in Fig. 4 and the representative TACs in Fig. 7. The number of voxels in the healthy, neoplastic, necrotic and splenic tissue ROIs are 1018, 226, 58 and 270, respectively.

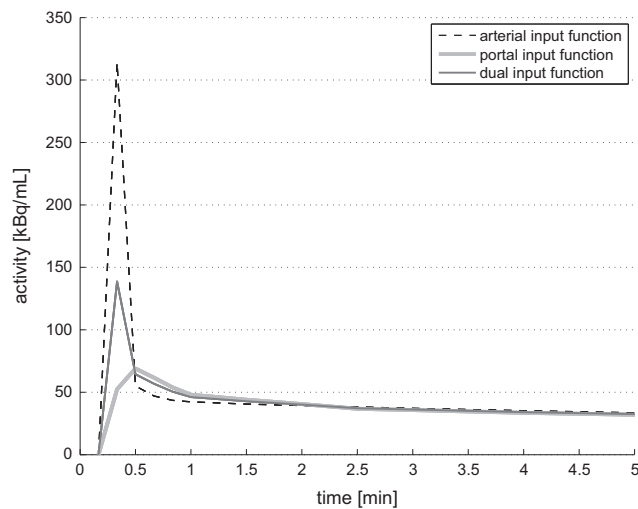
A dual hepatic artery-portal vein input function was used to compute the parametric images for liver voxels. An image-derived arterial input function  $c_a(t)$  was first obtained by averaging a core of voxels in the abdominal aorta. The portal input function  $c_p(t)$  was constructed from the arterial input function using the method proposed in Munk et al. (2003) and Winterdahl et al. (2011) with  $\beta = 0.5$ . As roughly one-third of blood flow to the liver is from the hepatic artery and two-thirds from the portal vein, the dual input function is  $c_d(t) = 0.33c_a(t) + 0.67c_p(t)$ . The value of the inverse of the mean residence time of blood for the liver used is, as discussed above,  $\alpha_{liver} = 5$ . The spleen is assumed to be roughly as vascular as the liver and perfused at one-and-a-half times the rate (Brown et al., 1997; Oguro et al., 1993), providing  $\alpha_{spleen} = 7.5$ . The arterial input function and  $\alpha = 7.5$  was used to compute the parametric image for all other voxels outside of the liver. The arterial, portal and dual blood input functions that are used to compute the parametric images are plotted in Fig. 5. The model solutions, grouped by compartment, are presented in Fig. 10a–f. Parametric images computed from the slice of PET data are shown in Fig. 11a–f. The standard model images are contained in the first column and the tubes images in the second.



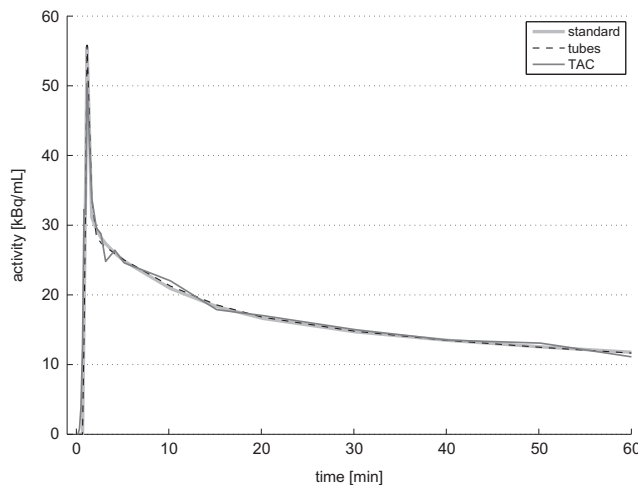
Fig. 3. Axial slice of static PET image through the liver and spleen.



Fig. 4. Tissue ROIs.



**Fig. 5.** Arterial, portal and dual blood input functions used to compute parametric images (only first 5 min shown).



**Fig. 6.** Standard and tubes model fits to a healthy liver TAC.

The optimisation problem for the tubes model is the same as the standard model, namely given a TAC in the form  $y(t_i) = y^i$  and weights  $w_i = 1/\sqrt{y^i}$ ,  $i = 1, \dots, N$ , we seek to minimise

$$\min_{k_1, k_2, k_3, f_b} \frac{1}{2} \sum_{i=1}^N \left( w_i [y^i - (1-f_b)(c_1^i(k_1, k_2, k_3, f_b) + c_2^i(k_1, k_2, k_3, f_b)) - f_b c_b^i(k_1, k_2, k_3, f_b)] \right)^2$$

over the reaction rates  $k_1, k_2, k_3$  and the fractional blood volume  $f_b$ , but notice now that the concentrations themselves also depend on  $f_b$  and that the blood concentration term is  $c_b$  rather than  $c_{b,in}$ .

The initial peak in the TACs corresponds to the arrival of the injected bolus of FDG. In a normal voxel, activity peaks and then decreases with the passing of the bolus. In contrast, in a neoplastic voxel, activity steadily increases after the passing of the bolus. In neoplastic tissue, FDG-6-P is retained in the second intracellular compartment, corresponding to rise in  $c_2$ , producing the distinctive profile of the neoplastic TAC in Fig. 7. The standard model solutions to a given TAC, whether normal or neoplastic, display the characteristic that the initial TAC peak is fitted more by  $c_1$  than  $f_b$ , producing a greater rise in  $c_1$ . On the other hand, the reverse is true for the tubes model, resulting in a more subdued rise in  $c_1$ . Simply put, the tubes model fits the initial TAC peak more through the peak in the blood

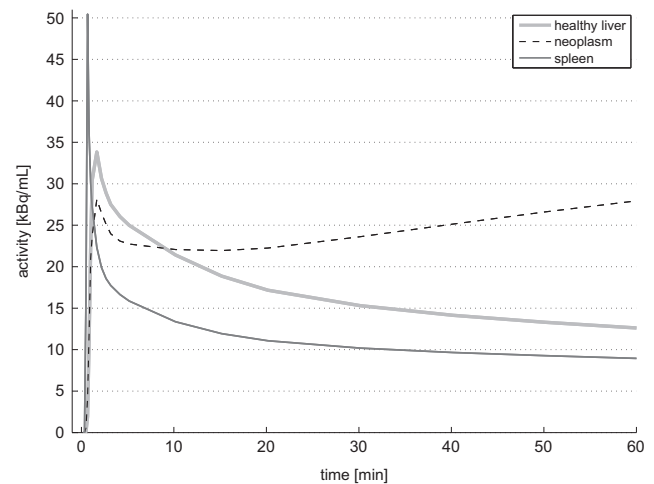


**Fig. 7.** Representative TACs for different tissue types.

input function than by a rapid rise of FDG concentration in the first intracellular compartment. This difference in model behaviour is apparent in all three tissue types, as shown in Fig. 10a–d, but is most marked in the spleen; compare Fig. 10b with Fig. 10c.

As the representative TACs are obtained by averaging many TACs in the regions of interest, hard-to-fit areas are smoothed, and the total fitted solution, that is  $(1-f_b)(c_1(t) + c_2(t)) + f_b c_b(t)$ , for both the standard and tubes models and the representative TACs essentially lie on top of each other. This suggests that, on the whole, both models produce total fits that fit TACs in all four regions of interest reasonably well. We use the term total fit to emphasise that while the total fits are similar, the relative contribution from each of the three compartments differs between the standard and tubes models, as just discussed and illustrated in Fig. 10a–f. The features of hard-to-fit TACs warrant further investigation, but for the moment it is instructive to examine the total fits in two neoplastic TACs. The standard and tubes model total solutions to two different individual neoplastic TACs are shown in Fig. 9. Both models fit the neoplastic TAC in Fig. 9a reasonably well, whereas both models struggle to fit the neoplastic TAC in Fig. 9b. The neoplastic TAC in Fig. 9b appears to display two stages of tracer metabolism following the passing of the bolus: tracer concentration is relatively constant until about the 30 min mark, at which point it begins to accumulate more rapidly. In contrast, tracer is seen to steadily accumulate almost immediately after the passing of the bolus in Fig. 9a. The simple linear reaction kinetics of both models is unable to account for the two different stages of uptake seen in the neoplastic TAC in Fig. 9b. This may suggest that more complex reaction kinetics are needed to appropriately model cancer biology in neoplastic TACs.

The influence of perfusion rate on average voxel blood concentration  $c_b(t)$  is shown in Fig. 8, where the tubes model is solved for a neoplastic TAC with perfusion rates of  $\alpha = 1$  and  $\alpha = 5$ . As can be seen, a decrease in perfusion rate results in greater dissipation of  $c_b(t)$ . Importantly, at the physiological value of  $\alpha = 5$ , the tubes model predicts a drop in blood concentration over the length of sinusoids. Conversely, as the perfusion rate increases, the drop in blood concentration across sinusoids diminishes, and the tubes model behaves more like the standard model. The brain is about 5% blood by volume and is perfused at a rate of 0.5 mL/min/g of brain, corresponding to  $\alpha_{brain} = 10$ . The assumptions of the standard model are therefore more appropriate for the brain than the liver.

The claim that the tubes model provides a more physiologically reasonable fit than the standard model is supported by experimental measurements of fractional blood volume and blood flow rate in the liver and spleen. The fractional blood volume and perfusion rate for

the liver and spleen computed using the standard and tubes model are presented in Table 1. Again, the perfusion rate is computed from the fractional blood volume by  $q = \alpha f_b$  mL/min/g of tissue. As discussed in Section 3, the tubes model assumes rapid equilibration of blood concentration between the intravascular compartment and the space of Disse. The blood compartment of the tubes model consists, therefore, of both the intravascular space and the extravascular space of Disse. The stated range for the average fractional blood volume of the liver of 25–30% refers to intravascular blood and not plasma in the space of Disse (Lautt, 2009; Arias et al., 2011). Furthermore, tagged albumin studies have shown that in the liver, albumin occupies a space up to 48% greater than the intravascular space, indicating that the space of Disse may be up to half the volume of the intravascular space (Goresky, 1963; Arias et al., 2011). This being the case, we expect that the value of  $f_b$  fitted by the tubes model may be higher than 0.25–0.30. As shown in Table 1, for healthy liver tissue the standard model predicts  $f_b = 0.20$  mL of blood/mL of voxel, which is slightly lower than average physiological range, and the tubes model predicts  $f_b = 0.31$  mL of blood/mL of voxel, which is slightly higher than physiological range. The low prediction of  $f_b$  by the standard model relative to experimental data is most apparent in the spleen, where the standard and tubes models predict  $f_b$  values of 0.08 and 0.23 mL of blood/mL of voxel, respectively, in comparison with experimental values in the

range 0.17–0.28. The low fractional blood volume predicted by the standard model is a consequence of the model's unphysiological assumption that there is no drop in blood concentration across a voxel, as well as its tendency to fit the TAC peak more with  $c_1$  than  $f_b$ .

Fractional blood volume and perfusion rate computed by the standard model are compared with experimental data in pigs by Munk et al. (2001). The standard model estimate of fractional blood volume in Munk et al. (2001) is 0.40 mL of blood/mL of voxel, which is higher than the figure we obtain here of  $f_b = 0.20$  mL of blood/mL of voxel in healthy liver. The major determinant of the computed value of  $f_b$  is the peak of the input function used to fit the data. The peak of the dual input function presented in Fig. 1 of Munk et al. (2001) is approximately 80 kBq/mL, whereas the dual input function we use, constructed from the image-derived arterial input function using the method of Munk et al. (2003), has a peak of 139 kBq/mL. The subjects imaged in Munk et al. (2001) are healthy pigs, whereas our PET data is from a patient diagnosed with metastatic liver disease. An advantage of performing PET imaging on animal subjects is that the portal vein can be sampled, whereas this is not practical with human patients, and the portal input function must be modelled from the arterial input function. The dual input function is computed from the arterial and portal input functions assuming that one-third of the blood supply to the liver is from the hepatic artery and the remaining two-thirds from the portal vein. Hepatic blood flow increases to contribute up to half of the liver's total blood supply in patient's with metastatic liver disease (Leen et al., 1993), which is why we assume a contribution of one-third of the total flow, being at the high end of the normal range of one-third to one-fifth. The greater the contribution of arterial blood to the dual input function, the higher the peak of the dual input function, and hence the lower the computed fractional blood volume. The low fractional blood volume fitted by the standard model relative to experimental data, consistent with our findings here, has also been observed in kinetic modelling of DCE-MRI brain data. This is discussed, for example, in Chapter six and illustrated in Fig. 6.6 of Baert et al. (2006), where the standard model incorrectly places activity from the cerebral blood compartment into the first intracellular compartment.

The differences between the standard and tubes model solutions influence the parametric images in two important ways. The second intracellular compartment is the compartment of most interest in identifying neoplastic liver lesions. The over-distribution of FDG to the first intracellular compartment distorts reaction kinetics by inappropriately making more FDG available for reaction in the

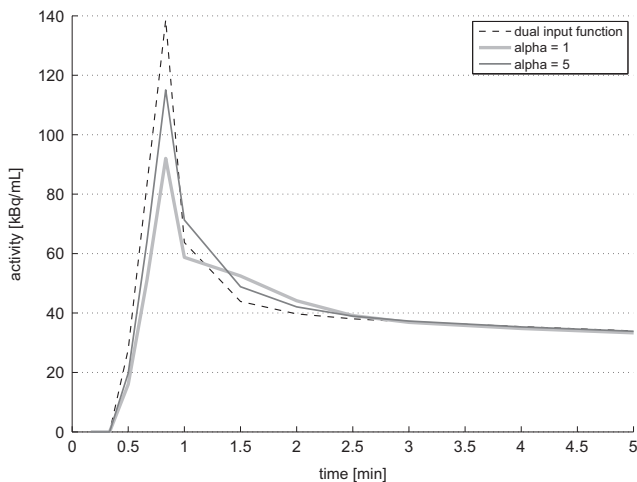


Fig. 8. Average voxel blood concentration  $c_b(t)$  for different perfusion rates (only first 5 min shown).

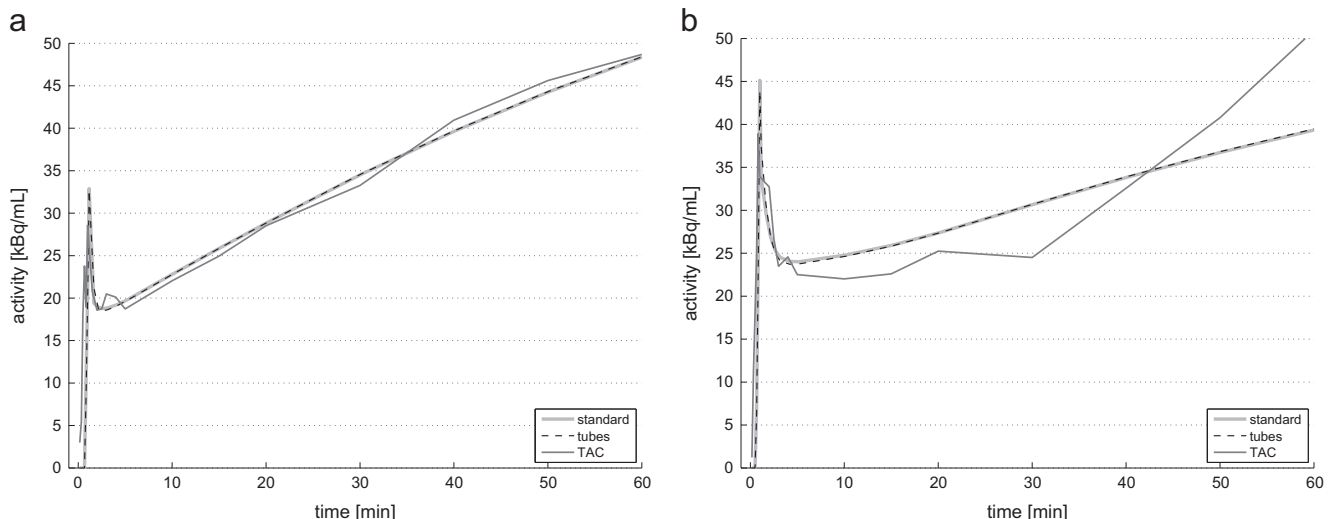
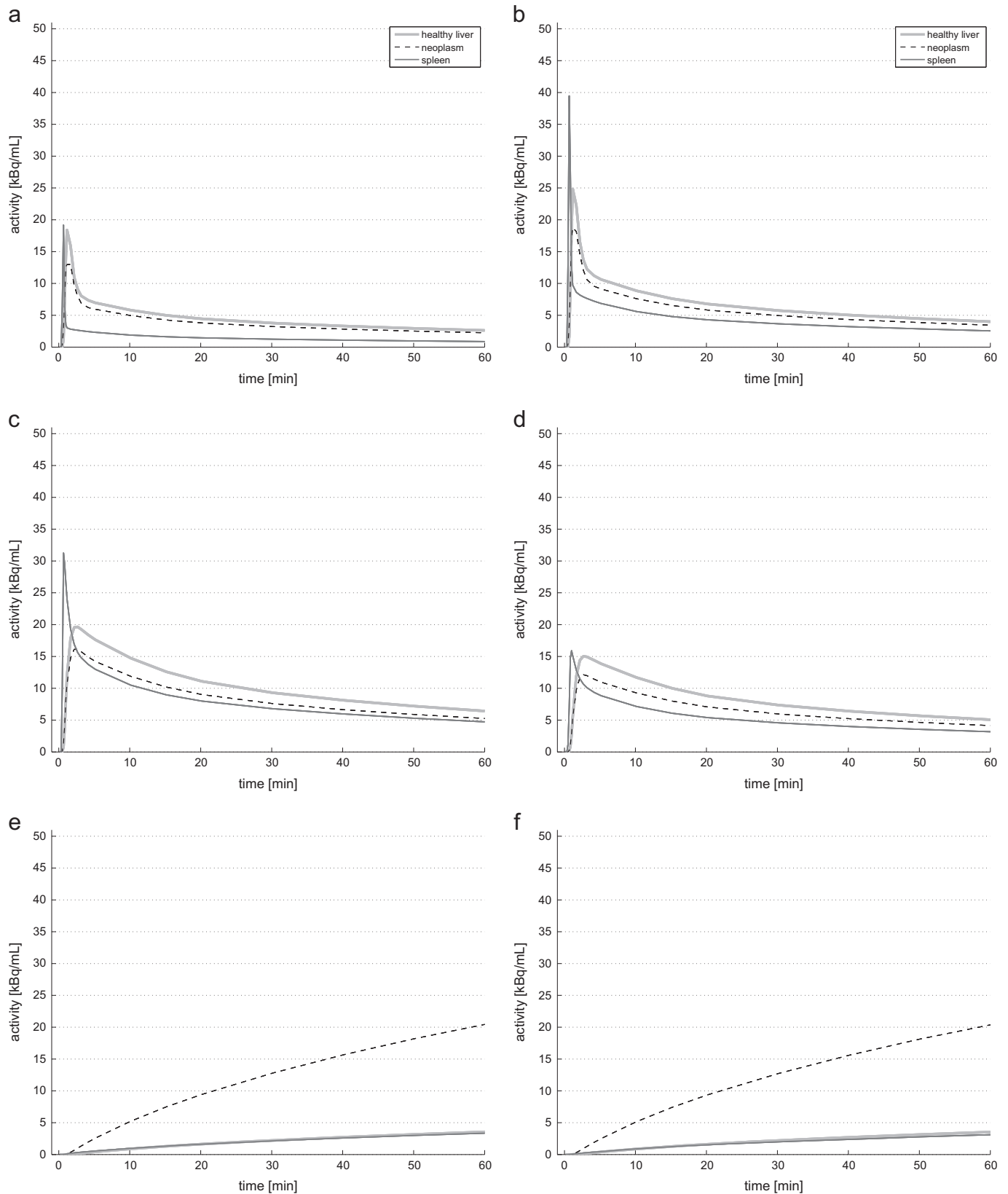


Fig. 9. Standard and tubes model fits to two different neoplastic TACs.





**Fig. 10.** Standard and tubes model solutions grouped by compartment for three different tissue types. (a) Standard model:  $f_b c_{b, in}(t)$ . (b) Tubes model:  $f_b c_b(t)$ . (c) Standard model:  $(1-f_b) c_1(t)$ . (d) Tubes model:  $(1-f_b) c_1(t)$ . (e) Standard model:  $(1-f_b) c_2(t)$ . (f) Tubes model:  $(1-f_b) c_2(t)$ .

second intracellular compartment. Secondly, the parametric images show that liver lesions are hypoperfused relative to surrounding healthy tissue, which is consistent with other measurements of

perfusion rate in liver tumours (Vaupel et al., 1989). As a result, kinetic parameters in hypoperfused lesions must be induced above kinetic parameters in equivalent normoperfused lesions in order to

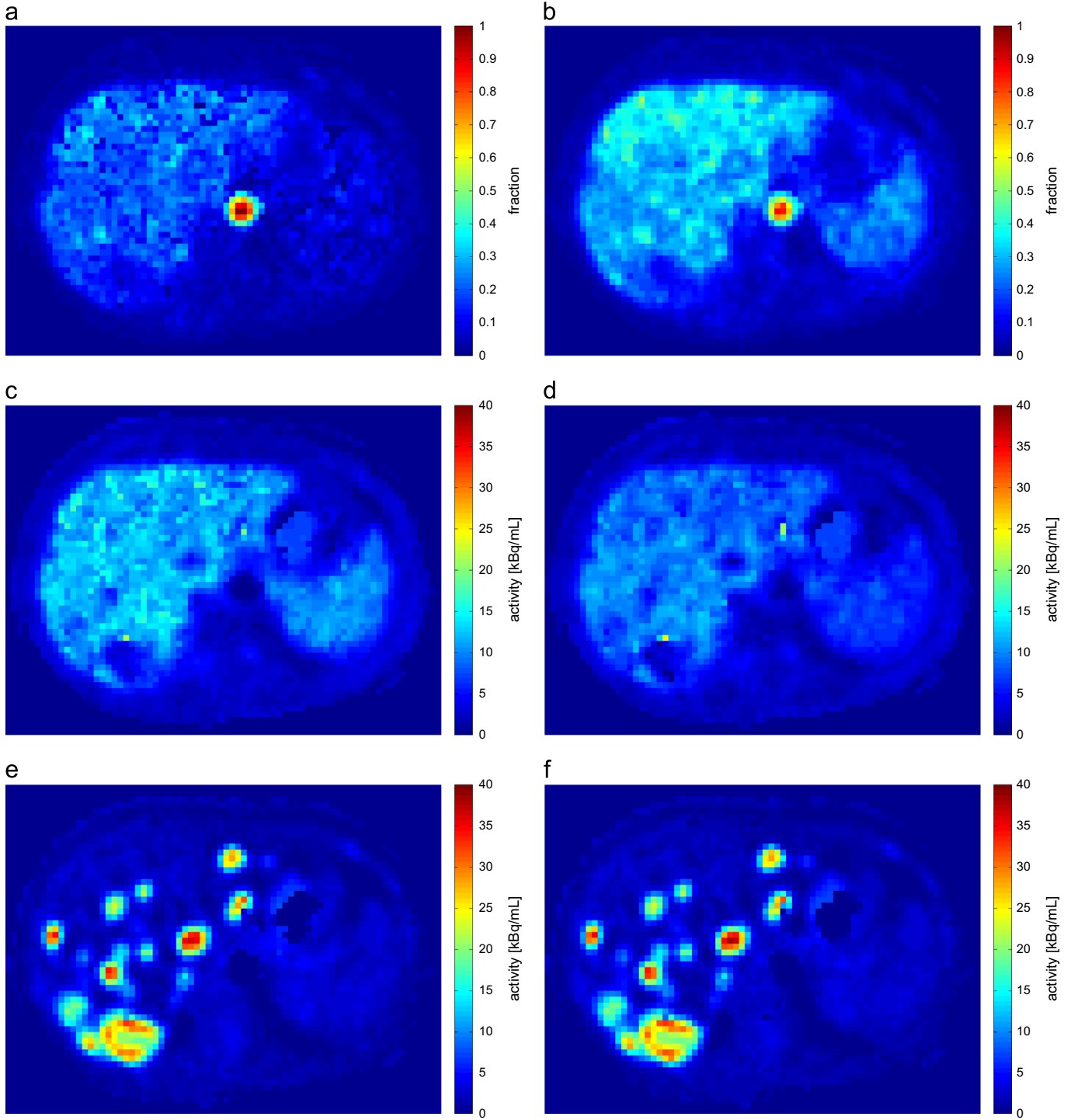


**Fig. 11.** Standard and tubes parametric images for a slice of PET data through the liver and spleen. (a) Standard model:  $f_b/T \cdot \int_t c_{b,m}(t) dt$ . (b) Tubes model:  $f_b/T \cdot \int_t c_b(t) dt$ . (c) Standard model:  $(1-f_b)/T \cdot \int_t c_1(t) dt$ . (d) Tubes model:  $(1-f_b)/T \cdot \int_t c_1(t) dt$ . (e) Standard model:  $(1-f_b)/T \cdot \int_t c_2(t) dt$ . (f) Tubes model:  $(1-f_b)/T \cdot \int_t c_2(t) dt$ .

account for increased metabolism in the presence of decreased perfusion. By its very assumptions, the standard model is unable to properly account for local changes in perfusion. The physiologically informed nature of the tubes model ultimately manifests in the parametric images as improved contrast between neoplastic and healthy liver tissue. In clinical practice, the primary utility of parametric images is to enable the rapid identification of regions of neoplasm within liver and to enable an accurate assessment of the biological factors relevant to establishing a prognosis for the patient. Two proxies for ease of identification and localisation of tumours are

image contrast, i.e. how distinctive the intensity in tumour is relative to healthy liver; and heterogeneity, i.e. how noisy intensities are within a particular organ. Contrast between the mean foreground (lesion) intensity  $\bar{I}_a$  and the mean background (healthy liver) intensity  $\bar{I}_b$  in compartment two was computed in a standard manner using the ratio of the difference between the mean intensities and the background intensity:  $|\bar{I}_a - \bar{I}_b| \cdot \bar{I}_b^{-1}$ . Heterogeneity within each region was quantified by computing the mean absolute intensity gradient:  $\int_X |\nabla I(x)| dx \cdot (\int_X dx)^{-1}$  (Kale et al., 2010). The contrast between neoplastic and healthy liver, and the

**Table 1**  
Fractional blood volume ( $f_b$ ) and perfusion rate ( $q$ ) for different tissue types computed using standard and tubes models. FBV is in mL of blood/mL of voxel, and perfusion rate  $q$  is in mL/min/g of tissue. Data are presented as *mean* (standard deviation).

Model	Fractional blood volume		
	Standard model	Tubes model	Literature values
Healthy liver	0.20 (0.06)	0.31 (0.07)	0.25–0.30 (Lautt, 2009; Arias et al., 2011)
Neoplasm	0.17 (0.05)	0.27 (0.06)	
Necrosis	0.11 (0.03)	0.15 (0.04)	
Total liver	0.19 (0.06)	0.29 (0.07)	0.17–0.28 (Brown et al., 1997; Oguro et al., 1993)
Spleen	0.08 (0.04)	0.23 (0.06)	
Model	Perfusion rate		
	Standard model	Tubes model	Literature values
Healthy liver	1.00	1.55	1.00–1.30 (Goresky, 1963; Arias et al., 2011)
Neoplasm	0.85	1.35	
Total liver	0.95	1.45	
Necrosis	0.55	0.75	1.68 (Brown et al., 1997; Oguro et al., 1993)
Spleen	0.60	1.73	

heterogeneity of healthy and neoplastic liver are presented in Table 2. The tubes model slightly improves over the standard model in terms of both contrast and heterogeneity. Both kinetic models substantially improve image contrast between neoplastic and healthy liver tissue over the static PET image.

Model fit residual considers only one facet of model appropriateness. As discussed in Section 2, we used the AIC to compare the standard model with reversible and irreversible kinetics, as well as the tubes model with irreversible kinetics. The AIC for a fitted model is given by  $AIC = N \log R + 2P$ , where  $N$  is the number of data points,  $R$  is the (weighted) residual, and  $P$  is the number of free model parameters (Akaike, 1998). Table 3 presents the AIC for standard and tubes model solutions in various ROIs. Of the standard models, in terms of the AIC, the more complex reversible model is less favourable than the irreversible model. The two irreversible models have very similar AIC values, with no model clearly outperforming the other. Model appropriateness cannot solely be judged on fit residual, as a successful model must not only fit the measured data, but it must also do so in a way such that the fitted model parameters are indicative of the underlying biology of the system being examined. Rather than a simple decrease in fit residual relative to the number of model parameters, as we have argued throughout, the improvement of the tubes model is a more physiologically faithful fit profile between the three compartments.

## 5. Concluding remarks

Application of kinetic analysis to PET of the liver presents the opportunity to move beyond tissue-generic standard models, initially developed for the brain, and develop compartment models informed by the liver's unique structure and function. The introduction of the dual input function by Munk et al. (2001, 2003) unveiled the importance of using a physiologically informed model in order to obtain more meaningful model parameters. The improvement of the tubes model over the standard is not a simple decrease in residual, but rather a more physiologically faithful profile of fits across the blood and intracellular compartments, which in turn, impacts the appearance of parametric images. As discussed in Section 4, there is the hint that existing dynamic PET scans possess sufficient resolution to attempt to model more complex reaction mechanisms present in neoplastic tissue.

The measurements of fractional blood volume, perfusion rate, image contrast and heterogeneity presented in this paper are

**Table 2**  
Measurements illustrating clinical utility. Desired attributes are high contrast and low heterogeneity.

Tissue	Static PET	Standard model	Tubes model
<b>Contrast</b>			
Neoplasm vs liver	0.53	4.16	4.27
<b>Heterogeneity</b>			
Neoplasm		23.3	23.2
Liver		5.7	5.6

**Table 3**  
Akaike Information Criterion for different models. Data are presented as *mean* (standard deviation).

Model	Akaike Information Criterion (AIC)		
	Irreversible standard model	Reversible standard model	Irreversible tubes model
Healthy liver	77.64 (15.71)	79.59 (15.75)	77.67 (15.29)
Neoplasm	76.36 (15.48)	78.31 (15.52)	76.42 (14.87)
Necrosis	73.75 (17.71)	75.69 (17.82)	73.87 (16.64)
Total liver	74.35 (17.19)	76.29 (17.25)	74.45 (16.68)

computed from a single slice of PET data. Given the success of the tubes model, work is currently being undertaken to investigate the tubes model on a larger cohort of complete abdominal scans, as well as to assess the clinical utility of tubes parametric images.

## Appendix A. List of symbols

$\alpha$	inverse of mean residence time
$\bar{\tau}$	mean residence time of blood in a voxel
$\bar{c}_s(t)$	average sinusoidal blood concentration
$\partial_t$	partial derivative with respect to $t$
$\partial_x$	partial derivative with respect to $x$
$\rho$	liver tissue density in g/mL
$A_s$	cross-sectional area of sinusoids
$A_{rxn}$	surface area available for GLUT2 transporters to occupy
$c_1(x, t)$	concentration in first intracellular compartment
$c_2(x, t)$	concentration in second intracellular compartment

$c_b(t)$	total voxel blood concentration
$c_s(x, t)$	concentration of blood in sinusoids
$c_{b,in}(t)$	concentration of blood flowing into sinusoids
$D$	diffusion coefficient of FDG in blood
$F$	total blood flow rate to a voxel in mL/min
$f_b$	fractional blood volume
$F_s$	blood flow rate to sinusoids in mL/min
$k_i, i = 1, \dots, 4$	reaction rate constants
$L$	length of sinusoids
$q$	total perfusion rate to a voxel in mL/min/g of tissue
$q_s$	perfusion rate to sinusoids in mL/min/g of tissue
$R$	radius of sinusoids
$S_s$	surface area of sinusoids
$v$	blood flow velocity in sinusoids
$V_b$	total blood compartment volume
$V_l$	volume of large blood vessels
$V_s$	volume of sinusoids
$V_{vox}$	total volume of a voxel
$w_i$	weights for model fitting

## Appendix B. Analytic solution of the tubes model

The blood input function can be well-approximated by a sum of exponential functions (Feng et al., 1993; Munk et al., 2003):

$$c_{b,in}(t) = \sum_i A_i e^{-\kappa_i t}. \quad (B.1)$$

The values of  $\kappa_i$  are determined by fitting the sum of exponentials to the measured blood input function using nonlinear least squares. Substituting (B.1) into (12), the solution of the sinusoidal blood concentration is

$$c_s(x, t) = e^{-at} \sum_i A_i e^{-\kappa_i(t-x/v)} + \sqrt{bc} \cdot e^{-dt} \sum_i A_i e^{\kappa_i x/v} \int_0^t e^{-(a-d+\kappa_i)\tau} \sqrt{\frac{\tau}{t-\tau}} \cdot I_1(\eta) d\tau, \quad (B.2)$$

where  $a, b, c, d$  and  $\eta$  are as defined in Section 4. We need the following integral identity (Hill, 1981):

$$\int_0^t e^{-\lambda\tau} \sqrt{\frac{\tau}{t-\tau}} \cdot I_1(\eta) d\tau = \frac{1}{\sqrt{bc}} \left\{ \left( \frac{\alpha e^{-at} - \beta e^{-\beta t}}{\alpha - \beta} \right) - e^{-\lambda t} \right\}, \quad (B.3)$$

where

$$\alpha = \frac{1}{2} \left( \lambda + \sqrt{\lambda^2 + 4bc} \right), \quad \beta = \frac{1}{2} \left( \lambda - \sqrt{\lambda^2 + 4bc} \right).$$

Making use of (B.3), Eq. (B.2) becomes

$$c_s(x, t) = e^{-at} \sum_i A_i e^{-\kappa_i(t-x/v)} + e^{-dt} \sum_i A_i e^{\kappa_i x/v} \left\{ \left( \frac{\alpha_i e^{-\alpha_i t} - \beta_i e^{-\beta_i t}}{\alpha_i - \beta_i} \right) - e^{-\lambda_i t} \right\}, \quad (B.4)$$

where  $\lambda_i = a - d + \kappa_i$  and

$$\alpha_i = \frac{1}{2} \left( \lambda_i + \sqrt{\lambda_i^2 + 4bc} \right), \quad \beta_i = \frac{1}{2} \left( \lambda_i - \sqrt{\lambda_i^2 + 4bc} \right).$$

Similarly, using the integral identity (Hill, 1981)

$$\int_0^t e^{-\lambda\tau} \cdot I_0(\eta) d\tau = \frac{e^{-\beta t} - e^{-at}}{\alpha - \beta}, \quad (B.5)$$

the solution for  $c_1(x, t)$  is found to be

$$c_1(x, t) = ce^{-dt} \sum_i A_i e^{\kappa_i x/v} \left( \frac{e^{-\beta_i t} - e^{-\alpha_i t}}{\alpha_i - \beta_i} \right).$$

## References

- Akaike, Hirotugu, 1998. Information Theory and an Extension of the Maximum Likelihood Principle, Selected Papers of Hirotugu Akaike, 1998, pp. 199–213.
- Anissimov, Yuri, 1998. Mathematical Modelling of Liver Kinetics (Ph.D. thesis).
- Anissimov, Y.G., Bracken, A.J., Roberts, M.S., 1997. Interconnected-tubes model of hepatic elimination. *J. Theor. Biol.* 188 (1), 89–101.
- Abramowitz, Milton, Stegun, Irene A., 1964. Handbook of Mathematical Functions: With Formulas, Graphs, and Mathematical Tables. Dover Publications, New York.
- Arias, Irwin, Wolkoff, Allan, Boyer, James, Shafritz, David, Fausto, Nelson, Alter, Harvey, Cohen, David, 2011. The Liver: Biology and Pathobiology. John Wiley & Sons, Chichester, West Sussex, UK.
- Brown, Ronald P., Delp, Michael D., Lindstedt, Stan L., Rhomberg, Lorenz R., Beliles, Robert P., 1997. Physiological parameter values for physiologically based pharmacokinetic models. *Toxicol. Ind. Health* 13 (4), 407–484.
- Baert, A.L., Jackson, Alan, Buckley, David L., Parker, Geoffrey, J.M., 2006. Dynamic Contrast-Enhanced Magnetic Resonance Imaging in Oncology. Springer Science & Business Media, Berlin.
- Bass, L., Keiding, S., Winkler, K., Tygstrup, N., 1976. Enzymatic elimination of substrates flowing through the intact liver. *J. Theor. Biol.* 61 (2), 393–409.
- Bass, L., Robinson, P., Bracken, A.J., 1978. Hepatic elimination of flowing substrates: the distributed model. *J. Theor. Biol.* 72 (1), 161–184.
- Carson, Richard E., 2005. Tracer Kinetic Modeling in PET. Positron Emission Tomography, pp. 127–159.
- Feng, D., Huang, S.C., Wang, X., 1993. Models for computer simulation studies of input functions for tracer kinetic modeling with positron emission tomography. *Int. J. Biomed. Comput.* 32 (2), 95–110.
- Goresky, Carl A., 1963. A linear method for determining liver sinusoidal and extravascular volumes. *Am. J. Physiol.* 204 (4), 626–640.
- Griffiths, Graham W., 2009. A Compendium of Partial Differential Equation Models: Method of Lines Analysis with Matlab. Cambridge University Press, Cambridge, New York.
- Hildebrand, Francis Begnaud, 1976. Advanced Calculus for Applications. Prentice-Hall, Englewood Cliffs, NJ.
- Hill, J.M., 1981. On the solution of reaction–diffusion equations. *IMA J. Appl. Math.* 27 (2), 177–194.
- Keiding, Susanne, 2012. Bringing physiology into PET of the liver. *J. Nucl. Med.* 53 (3), 425–433.
- Kale, K.V., Mehrotra, S.C., Manza, R.R.,
- Leen, E., Goldberg, J.A., Anderson, J.R., Robertson, J., Moule, B., Cooke, T.G., McArdle, C.S., 1993. Hepatic perfusion changes in patients with liver metastases: comparison with those patients with cirrhosis. *Gut* 34 (4), 554–557.
- Lautt, W. Wayne, 2009. Hepatic circulation: physiology and pathophysiology. In: Colloquium Series on Integrated Systems Physiology: From Molecule to Function to Disease. Morgan & Claypool Life Sciences, San Rafael (CA).
- Levenberg, Kenneth, 1944. A method for the solution of certain non-linear problems in least squares. *Q. J. Appl. Math.* 11, 164–168.
- Leenders, K.L., Perani, D., Lammertsma, A.A., Heather, J.D., Buckingham, P., Healy, M. J., Gibbs, J.M., Wise, R.J., Hatazawa, J., Herold, S., 1990. Cerebral blood flow, blood volume and oxygen utilization. Normal values and effect of age. *Brain: A Journal of Neurology* 113, 27–47.
- Munk, O.L., Bass, L., Roelsgaard, K., Bender, D., Hansen, S.B., Keiding, S., 2001. Liver kinetics of glucose analogs measured in pigs by PET: importance of dual-input blood sampling. *J. Nucl. Med.* 42 (May (5)), 795–801.
- Munk, Ole L., Keiding, Susanne, Bass, Ludvik, 2003. Impulse-response function of splanchnic circulation with model-independent constraints: theory and experimental validation. *Am. J. Physiol. Gastrointest. Liver Physiol.* 285 (October(4)), G671–G680.
- Munk, Ole L., Keiding, Susanne, Bass, Ludvik, 2012. Combining compartmental and microvascular models in interpreting dynamic PET data. In: Functional Molecular Imaging in Hepatology (open access), pp. 24–31.
- Munk, Ole Lajord., Keiding, Susanne, Bass, Ludvik, 2003. Capillaries within compartments: microvascular interpretation of dynamic positron emission tomography data. *J. Theor. Biol.* 225 (1), 127–141.
- Marquardt, D., 1963. An algorithm for least-squares estimation of nonlinear parameters. *J. Soc. Ind. Appl. Math.* 11 (June (2)), 431–441.
- Oguro, Atsushi, Taniguchi, Hiroki, Koyama, Hiroshi, Tanaka, Hiroki, Miyata, Keigo, Takeuchi, Kazumi, Inaba, Tadashi, Nakahashi, Hisamitsu, Takahashi, Toshio, 1993. Quantification of human splenic blood flow (quantitative measurement of splenic blood flow with  $H_2^{15}O$  and a dynamic state method: 1). *Ann. Nucl. Med.* 7 (4), 245–250.
- Phelps, M.E., Huang, S.C., Hoffman, E.J., Selin, C., Sokoloff, L., Kuhl, D.E., 1979. Tomographic measurement of local cerebral glucose metabolic rate in humans with (F-18)2-fluoro-2-deoxy-d-glucose: validation of method. *Ann. Neurol.* 6 (5), 371–388.
- Powell, M.J.D., 1970. A hybrid method for nonlinear equations. In: Numerical Methods for Nonlinear Algebraic Equations, pp. 87–114.
- Rostrup, Egill, Knudsen, Gitte M., Law, Ian, Holm, Sren, Larsson, Henrik B.W., Paulson, Olaf B., 2005. The relationship between cerebral blood flow and volume in humans. *NeuroImage* 24 (January (1)), 1–11.
- Roberts, M.S., Rowland, M., 1986. A dispersion model of hepatic elimination: 1. Formulation of the model and bolus considerations. *J. Pharmacokinet. Biopharm.* 14 (3), 227–260.



- Sourbron, S.P., Buckley, D.L., 2012. Tracer kinetic modelling in MRI: estimating perfusion and capillary permeability. *Phys. Med. Biol.* 57 (2).
- Sokoloff, L., Reivich, M., Kennedy, C., Rosiers, M.H. Des, Patlak, C.S., Pettigrew, K.D., Sakurada, O., Shinohara, M., 1977. The [<sup>14</sup>C]deoxyglucose method for the measurement of local cerebral glucose utilization: theory, procedure, and normal values in the conscious and anesthetized albino rat. *J. Neurochem.* 28 (5), 897–916.
- Sathiakumar, Chithradevi, Som, Seu, Eberl, Stefan, Lin, Peter, 2010. NEMA NU 2-2001 performance testing of a philips gemini GXL PET/CT scanner. *Australas. Phys. Eng. Sci. Med.* 33 (June (2)), 199–209.
- Tofts, Paul S., Brix, Gunnar, Buckley, David L., Evelhoch, Jeffrey L., Henderson, Elizabeth, Knopp, Michael V., Larsson, Henrik B.W., Lee, Ting-Yim., Mayr, Nina A., Parker, Geoffrey J.M., Port, Ruediger E., Taylor, June, Weisskoff, Robert M., 1999. Estimating kinetic parameters from dynamic contrast-enhanced t1-weighted MRI of a diffusable tracer: standardized quantities and symbols. *J. Magn. Reson. Imaging* 10, 3.
- Vaupel, Peter, Kallinowski, Friedrich, Okunieff, Paul, 1989. Blood flow, oxygen and nutrient supply, and metabolic microenvironment of human tumors: a review. *Cancer Res.* 49 (December), 6449–6465.
- Winterdahl, Michael, Keiding, Susanne, Sørensen, Michael, Mortensen, Frank Viborg, Alstrup, Aage Kristian Olsen, Munk, Ole Lajord, 2011. Tracer input for kinetic modelling of liver physiology determined without sampling portal venous blood in pigs. *Eur. J. Nucl. Med. Mol. Imaging* 38 (February(2)), 263–270.
- Weisiger, Richard A., Mendel, Carl M., Cavalieri, Ralph R., 1986. The hepatic sinusoid is not well-stirred: estimation of the degree of axial mixing by analysis of lobular concentration gradients formed during uptake of thyroxine by the perfused rat liver. *J. Pharm. Sci.* 75 (March(3)), 233–237.